Rotational and vibrational excitation in the large-angle scattering of Na^+ ions from N_2 molecules

H. Tanuma, S. Kita, and I. Kusunoki
Research Institute for Scientific Measurements, Tohoku University, 1-1 Katahira-Nichome, Sendai 980, Japan

N. Shimakura
General Education Department, Niigata University, Niigata 950-21, Japan

(Received 27 April 1988)

Differential scattering of Na^+ ions from N_2 molecules was studied at laboratory energies of $100 \leq E_{lab} \leq 350$ eV and scattering angles of $15° \leq \theta \leq 45°$. The energy-loss spectra were measured with the time-of-flight technique. The experimental results were analyzed by the classical trajectory calculation. The spectra measured at small angles show a typical double-peak structure, while at large angles the spectra are composed of the three peaks. The triple-peak structure can be explained in terms of the rainbow effect on the angular momentum transfer mechanism, by taking into account the direction of the final rotational angular momentum vector. A drastic structural change of the energy-loss spectra was observed around the reduced scattering angle of $\tau = 8$ keV deg, independent of the collision energy. This can also be attributed to the rainbow effect arising from vibrational excitation.

I. INTRODUCTION

Study of the energy-transfer mechanism in ion-molecular collisions is of considerable interest in connection with chemical-reaction dynamics, plasma physics, astrophysics, and surface science. Impulsive molecular collisions generally cause rotational, vibrational, and electronic excitations, and even molecular dissociation. Momentum transfer (rotational and vibrational excitations) is an important elementary process in inelastic molecular collisions, and has been investigated over a wide range of collision energy, up to a few keV. Nevertheless, our knowledge about the vibrorotationally inelastic collision mechanism is still far from being complete.

In the last ten years, experimental and theoretical studies of differential scattering involving rotationally inelastic collisions have been carried out extensively at thermal and suprathermal collision energies, and the rotational excitation mechanism at low energy is now well understood.[1-9] Inelastic molecular collision experiments have been achieved by employing supersonic nozzle beams with very low translational and rotational temperatures. The rotational rainbow, which was found in low-energy molecular-beam experiments,[2,10] has become an established phenomenon in the study of collision dynamics of rotational energy transfer under the repulsive potential.

The rotational rainbows are observed either in the final rotational-state distribution at a fixed scattering angle or in the angular dependence of the excitation cross sections for a particular rotational transition. Both observations give the same information about the potential surface. Here we will refer to the rainbow in the former case, which is closely related to the present study carried out at higher collision energies. In molecular collisions which result in rotational excitation extending over many levels, the final rotational state distribution for a certain angle shows a prominent peak around the highest rotational state j_r. This phenomenon is termed the rotational rainbow.[11] Approximating the interaction potential by a hard ellipsoid with an eccentricity $e \ll 1$, the rotational rainbow state j_r is given by[6,11,12]

$$j_r = 2\hbar^{-1}(2\mu E)^{1/2}(A-B)\sin(\Theta/2) , \quad (1)$$

where A and B are the major and the minor semiaxes of the hard shell, respectively, E and Θ are the collision energy and scattering angle in the center-of-mass (c.m.) system, respectively, and μ is the reduced mass of the colliding system. The quantity $(A-B)$ represents the anisotropy of the repulsive potential. For fixed collision energy and scattering angle, the rainbow state j_r is proportional to the product $\mu^{1/2}(A-B)$ and thus depends on the collision system. In Xe-CO_2 collisions with a large coupling parameter of $\mu^{1/2}(A-B)$, the normal rotational rainbow could not be observed distinctly in the energy-transfer spectra, but a specific multiple-collision rotational rainbow structure was found for the first time.[3] The normal single-collision rotational rainbow appears only in sudden molecular collisions.[13]

Differential inelastic scattering in molecular collisions at moderate energies is also investigated utilizing a crossed-beam technique with supersonic target beams to clarify the collisional conditions. The energy-loss spectra in Na^+-N_2 and Na^+-CO collisions measured previously at the collision energies $27 \leq E \leq 192$ eV showed a distinct structure of the rotational rainbow.[14,15] Very similar results have also been obtained in measurements of Li^+ ions scattered from N_2 and CO molecules at $4 \leq E \leq 17$ eV.[16] Rotational rainbows are thus observed not only in low-energy atom-molecule collisions, but also

in moderate-energy ion-molecule collisions. In a collision system with a large coupling parameter of $\mu^{1/2}(A-B)$, the angular momentum transfer plays quite an important role in the energy-transfer mechanism even when the collision energy is high enough to lead to other inelastic processes. Rotational rainbows have also been found in electron-molecule,[17] molecule-surface collisions,[18] and even in collisional dissociation,[19] as well as photodissociation.[20,21]

Vibrorotational excitation in the high-energy collisions has been studied at very small laboratory angles of $\theta \lesssim 5°$ and laboratory energies of $E_{\rm lab} \gtrsim 500$ eV.[22–24] According to the experimental results, the angular and energy dependences of the most probable energy loss could be scaled quite well with Sigmund's law,[25] which suggests that the reduced energy loss f depends only on the reduced scattering angle $\tau = E_{\rm lab}\theta$. The scaling function $f(\tau)$ determined experimentally shows an interesting collision-system dependence.[24]

In the previous work, total differential cross sections (DCS) in the laboratory frame for impulsive Na^+-N_2 and Na^+-CO collisions have been measured over a wide range of the scattering angle, $\theta < 90°$.[26] The measured DCS for the two systems shows a distinct cutoff structure due to a huge momentum transfer in the collisions. The energy dependence of the cutoff structure suggests that vibrational excitation as well as rotational excitation plays an important role in the energy-transfer mechanism at higher energies and larger scattering angles. All the earlier works concerning impulsive molecular collisions at large angles have been devoted to an investigation of energy transfer due to vibrational excitation.[27–32] The angular-momentum transfer mechanism in large-angle scattering under impulsive conditions and the vibrational excitation effect upon the large angular momentum transfer are not yet known. These have stimulated us to the study of the momentum-transfer mechanism in impulsive collisions at large angles.

Dissociative processes in Na^+-N_2 collisions have previously been studied by detecting the fragment N atoms for $E_{\rm lab} = 200$ and 350 eV, at various forward scattering angles θ.[19] The time-of-flight (TOF) spectra of the fragment N atoms measured at small laboratory angles provide information on energy transfer at large c.m. angles. No indication of electronic excitation was found in the N-atom spectra. This experimental result suggests that the contribution of electronic excitation can be neglected in Na^+-N_2 collisions at energies $E_{\rm lab} \leq 350$ eV. This collision system is, therefore, suitable to study the momentum transfer in large-angle scattering.

In this study, energy loss spectra in the Na^+-N_2 collisions were measured by means of the TOF technique at $100 \leq E_{\rm lab} \leq 350$ eV and $15 \leq \theta \leq 45°$. The observed spectra show three types of distinct structure which are due to dynamical effects on the momentum transfer. The angular and energy dependences of the spectra were analyzed with the classical trajectory (CT) calculation, which provides valuable information on the momentum-transfer mechanism.

This article is composed of five sections. In Sec. II experimental apparatus is described briefly and the measured energy-loss spectra are presented. In Sec. III analyses with the hard-shell model and with the CT method are given. Comparisons of the experimental results with the calculations are also made. Section IV is devoted to the discussions on the momentum-transfer mechanisms in the impulsive Na^+-N_2 collisions, and a summary is given in Sec. V.

II. EXPERIMENTAL DETAILS

A. Apparatus

The crossed-beam apparatus used in the present study has been described in detail previously.[33] A schematic drawing of the crossed-beam experiment is shown in Fig. 1. The apparatus consists of five chambers, a nozzle source followed by a collimation chamber, an ion source, a main chamber, and a detector chamber. These are evacuated differentially with turbo-molecular pumps. The two beams cross each other perpendicularly in the main chamber, and the particles scattered in the plane are detected by a secondary-electron multiplier in the detector chamber, which is rotatable around the scattering center in the main chamber. The primary Na^+ ion are formed by surface ionization of the aluminosilicate $Na_2O \cdot Al_2O_3 \cdot 2SiO_2$ on a heated platinum filament. The ions are accelerated to a desired energy, $100 \leq E_{\rm lab} \leq 350$ eV, with a lens system, and are collimated by two slits within an angular spread of approximately 0.5° full width at half maximum (FWHM). The target N_2 beam is injected into the collision volume as a pulsed supersonic beam, which is obtained by adiabatic expansion of the source gases through a nozzle of 0.1 mm diameter followed by a skimmer.[34] The stagnation pressure P_0 in the nozzle beam source is approximately 1200 Torr.

The kinetic energies of the scattered ions were analyzed with a TOF technique. For the TOF measurements the Na^+ ion beam is pulsed with a pair of condenser plates in front of the collimating slits.[35] The flight path length from the scattering center to the detector is ap-

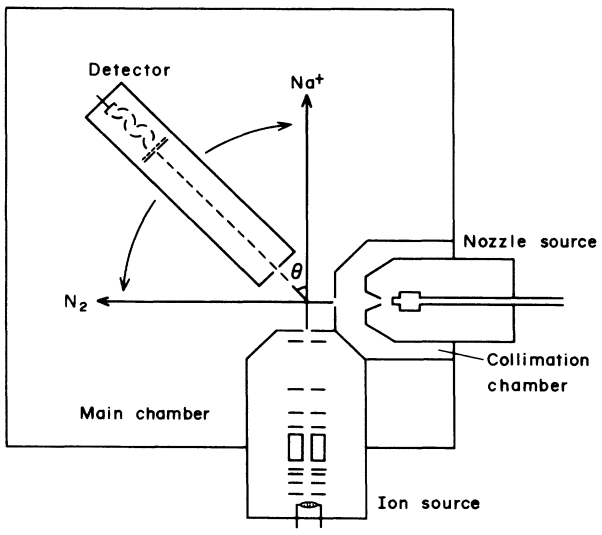

FIG. 1. Schematic drawing of the crossed-beam experiment.

proximately 50 cm. The overall angular resolution for the scattered particles is approximately 0.8° FWHM. The time resolutions $\Delta t/t$ in the TOF measurements at the scattering angles $\theta=20°$ and 40° are approximately 0.005 and 0.01, respectively. At large angles, the scattered ions distribute over a wide range of the flight time in addition to their low intensity. The experiments were, therefore, performed with angular and time resolutions worse than those employed in the previous works for small-angle scattering.[14,15]

In our apparatus the scattered ions and neutral species are detected simultaneously. According to the TOF analysis at $E_{lab} \leq 350$ eV, the neutral species detected are the fragment N atoms produced by collisional dissociation.[19] At small angles, $\theta \lesssim 30°$, the intensity of the neutral signal is much lower than that of the ions, while at large angles, $\theta > 30°$, the contribution of the neutral species to the total signal cannot be neglected. In this study a negative high voltage (~ -3 kV) is supplied to the first dynode of the secondary electron multiplier, so that the impinging energy of the ions is very much higher than that of the neutral species. Under this experimental condition, the pulse height of the secondary electron for the neutral species is approximately a factor of 3 lower than that for the ions. The neutral signal can, therefore, be cut off by a discriminator and only the ions are detected.

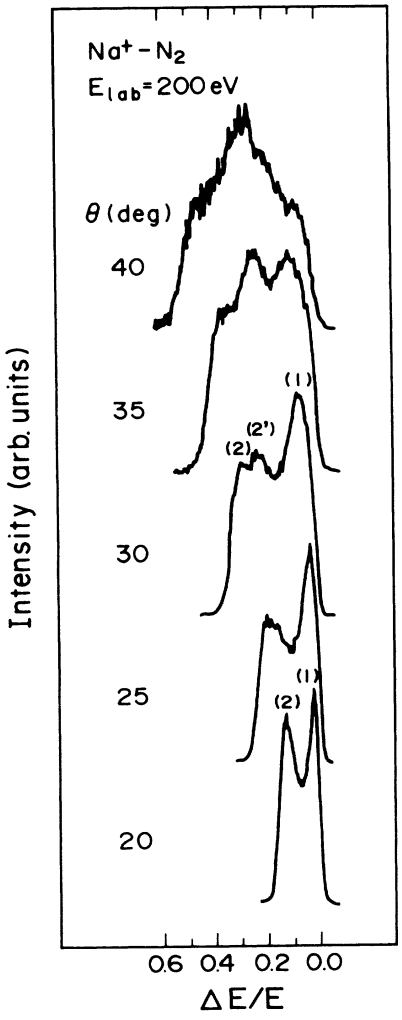

FIG. 2. Angular dependence of the experimental energy-loss spectra for Na^+-N_2 collisions at $E_{lab}=200$ eV.

B. Energy-loss spectra

Figure 2 shows the energy-loss spectra measured at $E_{lab}=200$ eV and $20 \leq \theta \leq 40°$. The abscissa in the figure is the reduced energy transfer $\Delta E/E$ in the c.m. frame, and the ordinate is the relative intensity normalized at the maximum in each spectrum. The energy-loss spectra $I(\Delta E/E,\theta)$ were deduced from the measured TOF spectra $I(t,\theta)$ with the relation $I(\Delta E/E,\theta)=I(t,\theta)dt/d(\Delta E)$, where t means the flight time. As is seen in the figure, the spectrum at laboratory angle $\theta=20°$ is composed of two peaks. This double-peak structure was discussed in the previous reports.[14,15] Peak (2) located at large energy transfer is due to the rotational rainbow effect, while peak (1) located near the elastic position is due to the rainbow effect arising from vibrational excitation in the collisions around the specific molecular orientation of $\gamma_c=90°$, where γ_c is the angle between the molecular axis and the intermolecular distance vector **R** at the turning point in the collisions. Increasing the scattering angle, the peaks broaden and shift to larger energy transfer, and peak (2) observed in the spectrum at $\theta=20°$ splits into two peaks (2) and (2') around $\theta=30°$. At larger angles of $\theta > 40°$, peaks (1) and (2) become less distinct and they are observed only as the shoulders of peak (2'). Thus the structure of the energy-loss spectra

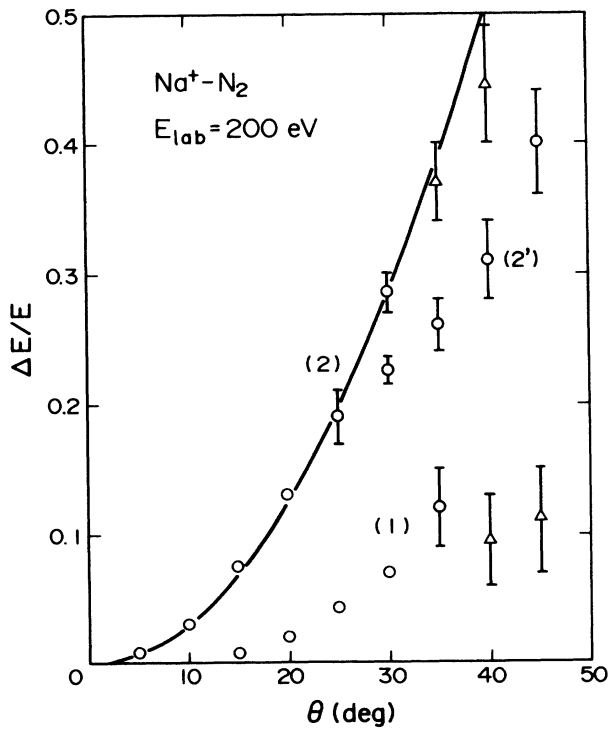

FIG. 3. Angular dependence of the reduced energy-loss positions of peaks (1), (2), and (2') observed in the spectra at $E_{lab}=200$ eV. The solid curve indicates the rotational rainbow positions determined by the hard-shell model.

depends strongly on the scattering angle. The angular dependence of the energy-loss position of each peak and shoulder at $E_{lab}=200$ eV is presented in Fig. 3. The open circles indicate the peak positions, while the open triangles denote the positions of shoulder.

The energy-loss spectra measured at the fixed angle of $\theta=35°$ and for several collision energies are shown in Fig. 4. In this figure, only the spectra measured at $150 \leq E_{lab} \leq 250$ eV are given. The overall structure of the spectrum observed at $E_{lab}=100$ V was almost the same as that for $E_{lab}=150$ eV, but the separation of peaks (2) and (2') was not as clear as for higher energies, which would be due to the lower signal-to-noise ratio in this spectrum. The spectra measured at higher energies of $275 \leq E_{lab} \leq 350$ eV were similar to the spectrum for $E_{lab}=250$ eV. The open circles and triangles in Fig. 5 show the collision-energy dependence of each peak position in the spectra measured at $\theta=35°$. The position of peak (2) in Fig. 5 depends only weakly on the collision energy. As shown in Fig. 4, however, the spectrum remarkably changes its structure around $E_{lab}=225$ eV. The structure in the spectra observed at a smaller angle of $\theta=20°$ was nearly independent of the collision energy and could be explained in terms of the rotational rainbow effect affected weakly by vibrational excitation.[14,15] The strong energy dependence of the spectra in Fig. 4 cannot be explained by rotational excitation only, and is considered to be due to the effect of vibrational excitation.

Figure 6 exhibits the angular dependence of the spectra measured at $E_{lab}=350$ eV. The spectra at $\theta=17.5°$ and 20° show the double-peak structure, while the typical structure disappears at $\theta=22.5°$ ($\equiv\theta_c$). As can be seen in Fig. 2, the similar change of structure in the spectra takes place around $\theta_c=40°$ for $E_{lab}=200$ eV, and in collisions at $E_{lab}=275$ eV the critical angle was $\theta_c \simeq 30°$. These results indicate that the angle θ_c depends on the collision energy, whereas the reduced angle $\tau_c=E_{lab}\theta_c=8$ keV deg is nearly independent of the energy.

As can be seen in Figs. 2, 4, and 6, the energy-loss spectra measured in this study show the three different types of structure; First is the typical double-peak structure (type I), second is the triple-peak structure (type II), and third is the single-peak structure with two shoulders (type III). Although the structure of type I is understood already,[14,15] the dynamical effects which bring about the structures of types II and III are not yet known. In Sec. IV we will discuss these effects on momentum transfer.

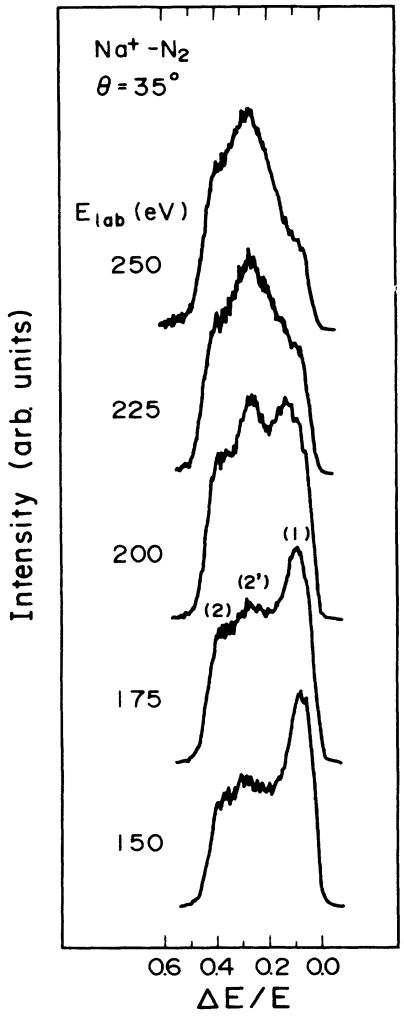

FIG. 4. Energy dependence of the experimental energy-loss spectra for Na^+-N_2 at $\theta=35°$.

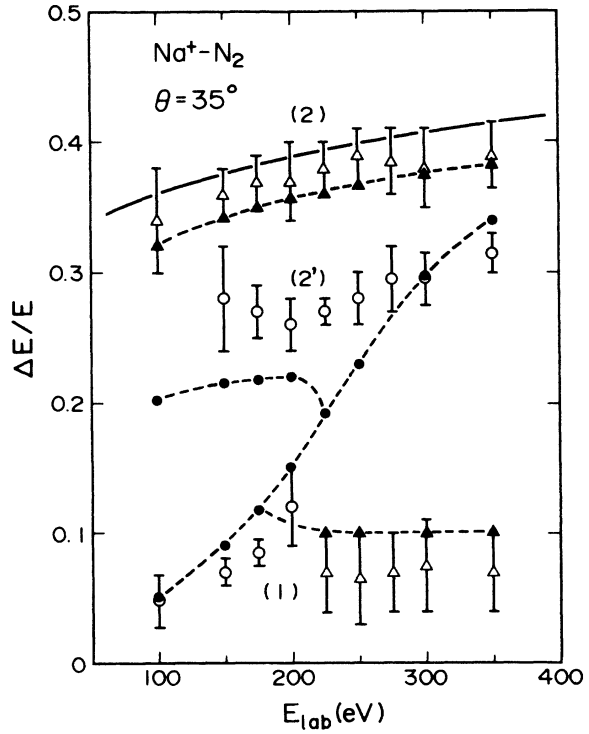

FIG. 5. Energy dependence of the reduced energy-loss positions of peaks (1), (2), and (2') observed in the spectra at $\theta=35°$. The open circles and triangles denote the experimental results. The solid curve indicates the rotational rainbow positions estimated with the hard-shell model. The solid symbols connected with the dashed curves exhibit the peak locations in the spectra obtained with the vibrotor CT calculation.

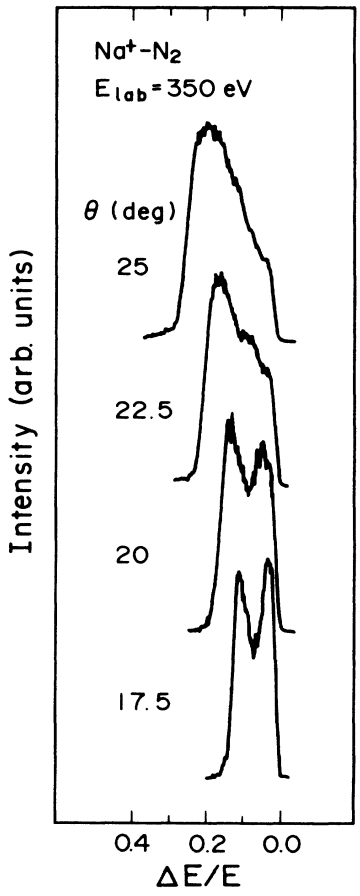

FIG. 6. Angular dependence of the experimental energy-loss spectra for Na^+-N_2 collisions at $E_{lab}=350$ eV.

III. COMPUTATION OF THE ENERGY-LOSS SPECTRA

A. Hard-shell model

The structure in the energy-loss spectra observed at small angles could be explained well with a simple hard-shell model for rotational excitation.[14,15] As the first step for understanding of the experimental results for large angle scattering, the energy transfer due to rotational excitation was computed with a hard-shell model to estimate the rotational rainbow position.

The hard-shell model,[12] which was successfully applied to small-angle scattering, is based on the infinite-order sudden approximation assuming a small energy transfer $\Delta E/E$. At large scattering angles, the energy transfer is so large that this hard-shell model becomes less reliable. The two-dimensional hard-shell model proposed by Bosanac,[6] on the other hand, has no such limitation on the energy transfer $\Delta E/E$. For large inelastic transitions most of the scattering occurs in a plane, so that the two-dimensional model is appropriate to estimate the highest rotational state (rotational rainbow state j_r) at a certain angle θ. In the present study, the Bosanac's hard-shell model is employed for the first evaluation of the experimental finding.

In the hard-shell model, rotational excitation is assumed to take place at the intermolecular distance $R^*(\gamma)$, i.e., the interaction potential $V(R,\gamma)=\infty$ for $R \leq R^*$ and $V(R,\gamma)=0$ for $R > R^*$. Here γ is the angle between the molecular axis and the vector **R**. The final rotational angular momentum quantum number j is given by[6]

$$j = 2\hbar^{-1} p_0 b_n \cos\phi/(1+b_n^2\mu/I) , \tag{2}$$

where p_0 is the initial linear momentum, b_n is the effective impact parameter, and ϕ is the incident angle on the shell surface. The quantities μ and I are the reduced mass of the system and the moment of inertia of the rigid rotor, respectively. If the shape of the hard potential shell $R^*(\gamma)$ is given, the rotational angular momentum $j(\gamma,\Theta)$ is calculated with Eq. (2) as a function of molecular orientation γ for a certain c.m. angle Θ.

In this calculation, the interaction potential for the collision system was approximated by the additive interaction

$$V(R,\gamma)=V(r_{12})+V(r_{31}) , \tag{3}$$

where the subscript 1 means Na^+ ion, 2 and 3 are constituent N atoms of the N_2 molecule, r_{12} and r_{31} are the interatomic distances, and R is the intermolecular distance. The intramolecular distance r_{23} is taken to be the equilibrium distance $r_e=1.098$ Å of the isolated N_2 molecule.[36] The Na^+-N interaction $V(r)$ are calculated with the statistical electron-gas model,[37] and was approximated in the exponential form

$$V(r)=A\exp(-Br) . \tag{4}$$

The potential parameters A and B were 1500 eV and 3.93 $Å^{-1}$, respectively. Under our experimental conditions, the effect of the attractive force can be neglected, and hence only the repulsive potential was taken into account. For the computation of the excitation function $j(\gamma,\Theta)$ with Eq. (2), one needs to know the shape of the hard-shell $R^*(\gamma)$ for each collisional condition. In this study, the function $R^*(\gamma)$ was assumed to be given by the equipotential surface, which is determined by the potential height at the turning point in the collisions following Hasegawa *et al.*[14]

1. Rotational rainbow positions

The excitation function $j(\gamma,\Theta)$, $0° \leq \gamma \leq 90°$ generally has a maximum value j_r ($\gg 1$) at a certain molecular orientation γ_r (in our case, $\gamma_r \simeq 50°$), and a minima ($j=0$) at $\gamma=0°$ and 90°. The rotational cross section $\sigma(j,\Theta)$ is nearly proportional to the Jacobian factor $D = |\partial j(\gamma,\Theta)/\partial\gamma|^{-1}$.[11] The quantity D is 0 at γ_r and has finite values at $\gamma=0°$ and 90°. The cross sections are, therefore, extremely large around the specific rotational angular momentum j_r, which is the rotational rainbow state. The rotational rainbow positions in the energy-loss spectra are given by $\Delta E_r = B_{rot} j_r(j_r+1)$, B_{rot} being the rotational constant.

The solid curves in Figs. 3 and 5 denote the rotational rainbow positions calculated with the hard-shell model.

These curves reproduce fairly well the angular and energy dependences of peak (2). This indicates that the largest energy loss in the spectra is due to angular momentum transfer, and peak (2) can be ascribed to the rotational rainbow.

B. Classical-trajectory calculation

The energy-loss spectra were calculated with the CT method to investigate the momentum-transfer mechanisms in more detail. In the CT calculation, Hamilton's equations for the three-body system described in terms of generalized coordinate are integrated numerically on the basis of a soft potential.[38,39] The c.m. scattering angle Θ and the energy ΔE transferred into the internal degrees of freedom of the molecule are evaluated from the initial relative velocity vector $\mathbf{v}_0$ and the final velocity vector $\mathbf{v}_1$. The final rotational angular momentum j is given by

$$j(j+1)\hbar^2 = |\mathbf{r}_{23}\times\mathbf{P}_{23}|^2 , \quad (5)$$

where $\mathbf{P}_{23}$ is the momentum vector conjugate to the intramolecular distance vector $\mathbf{r}_{23}$.

Interaction potential for the collision system was approximated by

$$V(r_{12},r_{23},r_{31}) = V(r_{12})+V(r_{23})+V(r_{31}) . \quad (6)$$

Here the potentials $V(r_{12})$ and $V(r_{31})$ are the same as those in Eq. (3). The intramolecular potential $V(r_{23})$ for a N_2 molecule is represented by a Morse potential

$$V(r) = D_e\{1-\exp[-a(r-r_e)]\}^2 , \quad (7)$$

where D_e is the well depth and a is the steepness of the potential. The values are $D_e = 9.91$ eV and $a = 2.69$ Å^{-1} for the isolated N_2 molecule.[36]

The collision geometry employed in this calculation is shown in Fig. 7. The initial velocity vector $\mathbf{v}_0$ lies in the x-y plane and is antiparallel to the x axis, and b represents the impact parameter. The center of the molecule is on the origin. The quantities α and β are the polar and azimuthal angles, respectively, defining the molecular orientation in the space fixed coordinate system. The molecule was assumed to be initially nonrotating and stationary at the intramolecular distance of $r_{23} = r_e$.

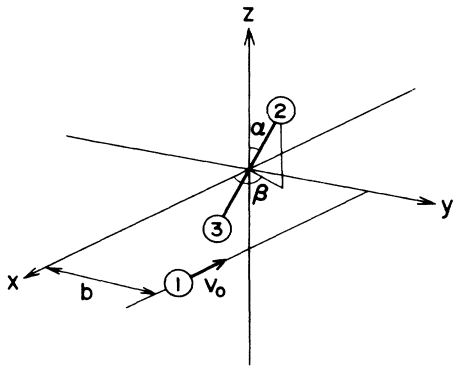

FIG. 7. Collision geometry employed in the CT calculation.

1. Rigid-rotor model

The computation with the hard-shell model indicates that the angular momentum transfer is the most important energy-transfer process even at large angles. As the second step of evaluation, the CT calculation of the energy-loss spectra was done with the rigid-rotor model, in which the vibrational freedom of the molecule is frozen. This model provides the significant insight into the angular-momentum-transfer mechanism. The Lagrange equations of motion in the rigid-rotor model are given by[38]

$$\ddot{\mathbf{R}} = -(1/\mu)\nabla_R V, \quad \ddot{\mathbf{r}} = -(1/m)(\nabla_r V - \lambda\mathbf{r}) ,$$

with

$$\lambda = (1/r^2)(\mathbf{r}\cdot\nabla_r V - m\dot{\mathbf{r}}\cdot\dot{\mathbf{r}}) , \quad (8)$$

where R and r are the intermolecular and intramolecular distances, respectively, and μ and m are the reduced masses of the collision system and of the N_2 molecule, respectively. λ is the Lagrange multiplier which represents the rigid-rotor constraint $r = r_e$.

Figure 8(b) shows the energy-loss spectrum calculated with the rigid-rotor model for the Na^+-N_2 collisions at $E_{lab} = 175$ eV and $\theta = 35°$. In this calculation, the spectrum was composed of about 2000 trajectories which fell into an angular window of $\Delta\theta = 0.4°$ centered at the laboratory angle of $\theta = 35°$. The computed spectrum was convoluted using a Gaussian function with an energy width of $\Delta(\Delta E/E) = 0.04$ (FWHM), which is somewhat larger than the experimental resolution of $\Delta(\Delta E/E) \simeq 0.025$ (FWHM). As can be seen in Fig. 8, the theoretical spectrum shows the triple-peak structure and reproduces satisfactorily the experimental spectrum in Fig. 8(a).

The spectra computed for $E_{lab} = 150$ and 200 eV at $\theta = 35°$ also show the triple-peak structure, and are almost the same as that for $E_{lab} = 175$ eV. The spectrum simulated for $E_{lab} = 150$ eV represents well the corre-

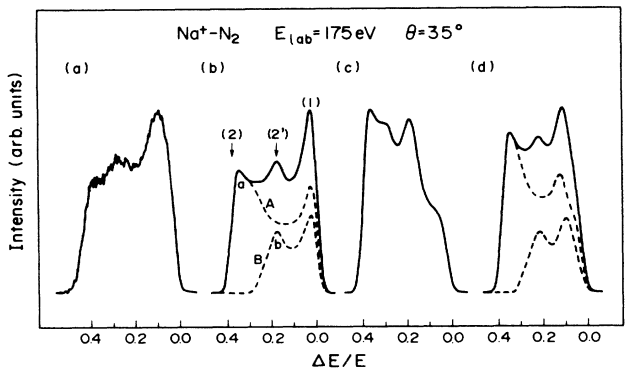

FIG. 8. Comparison of the experimental and calculated energy-loss spectra at $E_{lab} = 175$ eV and $\theta = 35°$. (a) Experimental spectrum; (b) calculation with the rigid-rotor model; and (c) and (d) calculations with the vibrotor model for $a = a_0$ and $2a_0$, respectively. The dashed curves in (b) and (d) exhibit the spectra separated according to the signs of j_z, which is the z component of the rotational angular momentum vector.

sponding experiment in Fig. 4, while the agreement between the computation and experiment at $E_{lab}=200$ eV is not so good as for the lower energies.

Figure 9 exhibits the spectra for $E_{lab}=250$ eV and $\theta=35°$; (a) is the experiment and (b) is the calculated spectrum. This simulated spectrum also shows the same structure as that of Fig. 8(b) for $E_{lab}=175$ eV, and does not reproduce the experiment of Fig. 9(a). It is noteworthy that the energy-loss positions of peak (2) in the calculated spectra always agree quite well with the experiments and with the rainbow positions obtained by the hard-shell model.

2. *Vibrotor model*

The energy-loss spectra computed with the rigid-rotor model at $100 \leq E_{lab} \leq 350$ eV and $\theta=35°$ are nearly independent of the collision energy, and do not interpret the energy dependence of the experimental spectra in Fig. 4. As the third step, the CT calculation with the vibrotor model[39] was carried out to reproduce the experimental spectra. The Lagrange equations of motion for the vibrotor model, which takes account of the vibrational freedom as well as the rotational freedom of the molecule, are equivalent to those with $\lambda=0$ (without the rigid-rotor constraint $r=r_e$) in Eq. (8).

Figure 8(c) shows the spectrum computed with the vibrotor model for the collisions at $E_{lab}=175$ eV and $\theta=35°$. The largest energy loss in the spectrum is almost the same as those in Figs. 8(a) and 8(b). Prominent peak (1) located around the elastic position in the experimental spectrum [Fig. 8(a)] cannot be, however, seen in the spectrum of Fig. 8(c). As mentioned above, peak (1) is affected by vibrational excitation on the collisions around the molecular orientation $\gamma_c=90°$. The disagreement between the computation [Fig. 8(c)] and the experiment [Fig. 8(a)], therefore, suggests that the model potential used in the calculation gives a vibrational excitation at $\gamma_c \simeq 90°$ that is too large.

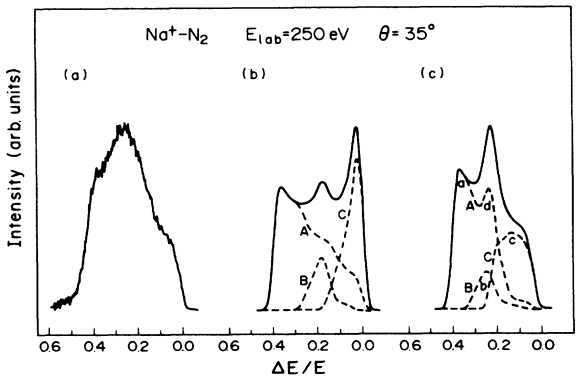

FIG. 9. Comparison of the measured and calculated energy-transfer spectra at $E_{lab}=250$ eV and $\theta=35°$. (a) Experimental spectrum and (b) and (c) calculations with the rigid-rotor and vibrotor models, respectively. The dashed curves in (b) and (c) exhibit the partial spectra. Curve *A*, single collisions with positive j_z; curve *B*, single collisions with negative j_z; and curve *C*, double collisions.

In order to get a better agreement with the experiment, we performed the CT calculations with other potential functions. One is the CT calculation with a modified potential,

$$V(r_{12},r_{23},r_{31})=(1-\delta)[V(r_{12})+V(r_{31})] + V(r_{23})+\delta V(R)\ , \tag{9}$$

where $V(R)$ is a spherical potential averaged over the molecular orientation γ and is obtained from Eq. (3). In this model potential, the potential anisotropy is adjusted by the parameter δ. When we chose $\delta=0.2$, prominent peak (1) in the spectrum of Fig. 8(a) could be reproduced satisfactorily. Peak (2) located around the largest energy loss in the spectrum, however, shifted to the energy transfer approximately 40% lower than that of the calculation for $\delta=0$. Therefore the computed spectrum showed a structure remarkably different from the experiment at larger energy losses. As discussed in Sec. III A, peak (2) in the experimental spectrum of Fig. 8(a) is due to the rainbow effect on rotational excitation. The energy-loss position of the rotational rainbow depends strongly on the potential anisotropy, which can also be seen in Eq. (1). Increasing the parameter δ, the potential anisotropy decreases, so that rainbow peak (2) shifts to the lower energy loss. The hard-shell-model calculation with $\delta=0$ reproduces well the location of experimental peak (2). One can conclude, therefore, that the disagreement concerned with peak (1) between the experiment and the calculation is not due to the inadequate potential anisotropy.

The other CT calculation was carried out by varying the steepness parameter a in the intramolecular potential of Eq. (7). With the increase of the parameter a, the structure around the elastic position could be better reproduced. The spectrum of Fig. 8(d) is the result computed with $a=5.38$ Å^{-1}, which is twice as large as the steepness of $a=2.69$ Å^{-1} ($\equiv a_0$) for the isolated N_2 molecule. As can be seen, this spectrum reproduces well the experiment of Fig. 8(a). We performed the CT calculation on the angular and energy dependences of the spectra by assuming the identical steepness of $a=2a_0$. It should be noted that the steepness a, which provides the best result of the computed energy-loss spectra, depends on the intermolecular distance R and on the orientation angle γ, in the strict sense.

Figure 9(c) exhibits the spectrum obtained with the vibrotor calculation for $E_{lab}=250$ eV and $\theta=35°$. The spectrum shows a prominent peak in the middle and reproduces the experiment of Fig. 9(a). The two spectra calculated with the rigid-rotor model [Fig. 9(b)] and with the vibrotor model [Fig. 9(c)] are distinctly different, which is due to the effect of vibrational excitation. Nevertheless, the gross features of the angular momentum j distributions $I(j)$ in these two calculations are still almost the same. Figure 10 exhibits the energy-loss spectra computed as a function of the collision energy E_{lab} at the fixed laboratory angle of $\theta=35°$. The spectrum changes distinctly its structure around $E_{lab}=225$ eV, which agrees with the experimental finding in Fig. 4. The solid symbols in Fig. 5 denote the energy dependence of the

peak positions in the computed spectra in Fig. 10. The agreement between the calculation and the experiment is fairly good. The angular dependence of the energy-loss spectra for $E_{lab}=275$ and 350 eV was also calculated. The spectra simulated for $E_{lab}=275$ and 350 eV vary their structure drastically around $\theta_c=30°$ and 22.5°, respectively. These theoretical results give the critical reduced angle $\tau_c=E_{lab}\theta_c\simeq 8$ keV deg, which is equal to the experimental value. Thus the vibrotor-model calculations by assuming the steepness of $a=2a_0$ explain fairly well the overall features of the angular and collision-energy dependences of the experimental spectra. This indicates that the dependence of the steepness a on the distance R is less significant under our experimental condition, $R\lesssim 1.5$ Å, which corresponds approximately to the intermolecular distance of the closest approach at the smallest reduced angle of $\tau=1.5$ keV deg in our experiment.

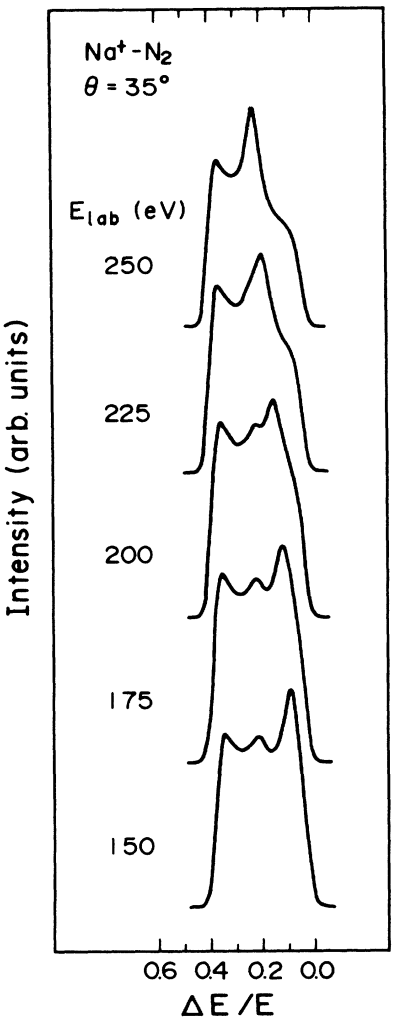

FIG. 10. Energy dependence of the spectra calculated with the vibrotor CT method at $\theta=35°$.

IV. MOMENTUM-TRANSFER MECHANISM

A. Angular momentum transfer

The two calculated spectra of Figs. 8(b) and 8(d) both show similarly triple-peak structure and reproduce satisfactorily the experiment of Fig. 8(a). Peak (2), which is ascribed to the rotational rainbow, is located at nearly the same energy loss in the theoretical two spectra. Both peaks (1) and (2′) in Fig. 8(d) are located at the energy transfer slightly higher than the corresponding peaks in Fig. 8(b). The shift of peak (1) was discussed already in the previous reports in detail.[14,15] The two rotational state distributions $I(j)$ determined from the trajectories, which compose the energy-loss spectra of Figs. 8(b) and 8(d), are almost the same. Consequently, the shift of peak (2′) in the energy-transfer spectra of Fig. 8(d) is due to the effect of vibrational excitation as similar to the shift of peak (1). Additional peak (2′) in the spectra is considered to originate from angular momentum transfer, so we will discuss here this mechanism in the large-angle scattering.

1. Rainbow effect

According to the three-dimensional CT calculation, the classical excitation cross section $\sigma(\Delta E,\theta)$ is given by[14,15]

$$\sigma(\Delta E,\theta)=A\sum_i \sin\gamma_{ci}\,|\,d(\Delta E)/d\gamma_c\,|_i^{-1}\,, \tag{10}$$

where A is a proportional constant and the summation is made over all branches of the excitation function $\Delta E(\gamma_c)/E$ which contribute to the same $\Delta E/E$. The classical cross sections diverge around the extrema of the function $\Delta E(\gamma_c)/E$, because of the Jacobian factor $|\,d(\Delta E)/d\gamma_c\,|^{-1}$. This is considered to be the rainbow effect on momentum transfer. The characteristic structures in the energy-transfer spectra are interpreted in terms of the rainbow effect. One can approximately separate the momentum transfer into angular and linear momentum transfers. The former corresponds to rotational excitation and the latter to vibrational excitation. The rainbow on the angular momentum transfer is the same with the rotational rainbow.

For the collisional geometry of Fig. 7, the total angular momentum vector **J** of the colliding system, which is equal to the initial orbital angular momentum vector $\mathbf{L}=\mu(\mathbf{b}\times\mathbf{v}_0)$, is parallel to the z axis. First, we will consider the in-plane scattering for the orientational angle $\alpha=90°$ in Fig. 7. A schematic drawing of the two different trajectories, which lie in the x-y plane, for a certain scattering angle θ is shown in Fig. 11. In the case of Fig. 11(a), the molecular orientation γ_c at the closest approach is positive and the final rotational angular momentum vector **j** is parallel to the z axis. For the collision in Fig. 11(b), the molecular orientation γ_c is negative and the angular momentum vector **j** is antiparallel to the z axis. Thus there exists two different mechanisms of angular momentum transfer in the in-plane scattering. Figure 12 denotes the reduced energy transfer $\Delta E/E$ as a

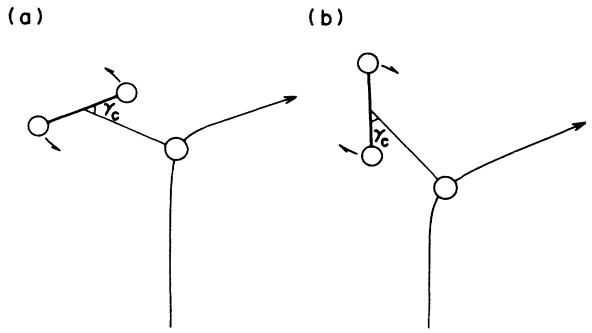

FIG. 11. Schematic drawing of the typical two trajectories for in-plane scattering, $\alpha=90°$, at a certain angle θ. In (a) both γ_c and j_z are positive, while in (b) they are negative.

function of the molecular orientation γ_c computed with the rigid-rotor model for the in-plane scattering. This excitation function shows two maxima.

If one assumes that the relation of Eq. (10) holds in the two-dimensional analysis, peaks (2) and (2′) in the spectrum of Fig. 8(b) can be attributed to the rainbow effect at the two maxima in the function of Fig. 12. The arrows in Fig. 8(b) indicate the rainbow positions determined from the excitation function of Fig. 12. As shown, the simple estimation based on the two-dimensional scattering model well explains the peak positions in the energy-loss spectrum.

The computed spectrum in Fig. 8(b) is composed actually of trajectories for three-dimensional scattering. As the next step, then, the trajectories were sorted according to the signs of j_z, which is the z component of the final angular momentum vector j. The dashed curve A in Fig. 8(b) shows the partial spectrum which is composed of the

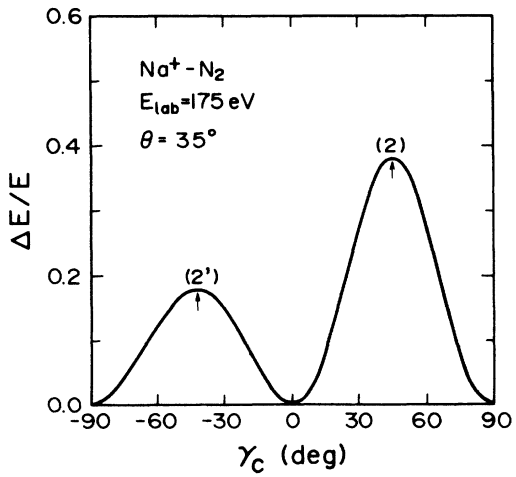

FIG. 12. Excitation function $\Delta E(\gamma_c)/E$ for in-plane scattering, $\alpha=90°$, determined with the rigid-rotor model at $E_{lab}=175$ eV and $\theta=35°$. The quantity γ_c is the molecular orientation angle at the closest approach.

trajectories of $j_z \geq 0$, and curve B for $j_z < 0$. The peaks a and b located around the largest energy loss in each curve are due to the rainbow effects. As can be seen in the figure, peaks (2) and (2′) in the spectrum are ascribed to rainbow peaks a and b, respectively. A similar analysis at other angles indicates that the energy separation $\Delta(\Delta E)_{ab}$ between peaks a and b increases as a function of scattering angle θ. At smaller angles, therefore, the two peaks are observed only as a single-peak in the energy-loss spectra as shown in Figs. 2 and 3. Two peaks (2) and (2′) in the spectrum of Fig. 8(d) computed with the vibrotor model are also ascribed to the rainbows. The triple-peak structure in the spectra, thus, is due to the splitting of a normal rotational rainbow, which is a new phenomenon observed on the angular momentum transfer.

2. *Split of the rotational rainbow*

The angular momentum transfer is treated very often with the hard-shell model. The splitting of the rotational rainbow peak cannot be explained with this simple model, in which both collisions for the molecular orientations $\gamma_c > 0°$ and $\gamma_c < 0°$ are equivalent. In order to investigate the energy difference between two maxima (2) and (2′) in Fig. 12, the two trajectories at $\gamma_c \simeq \pm 45°$, which are indicated with arrows in Fig. 12, are analyzed in detail. The initial azimuthal angles β of the trajectories for $\gamma_c \simeq 45°$ and $-45°$ are 105° and 10°, respectively. Figure 13 shows the time dependence of the two selected classical trajectories. The solid curves indicate the collisional parameters of the trajectory for $\gamma_c \simeq 45°$ (trajectory 1) and the broken curves are those of the trajectory for $\gamma_c \simeq -45°$ (trajectory 2). Here the origin of the time scale, $t=0$, is taken at the maximum of the interaction potential $V(t)$, and the time unit is 10^{-15} s. As shown in Fig. 13(b), the time dependences of the potential $V(t)$ for these two trajectories are almost the same. The time dependence of the molecular orientation $|\gamma(t)|$ is shown in Fig. 13(c). The function $\gamma(t)$ for trajectory 1 takes a minimum around $t=0$, while the function $-\gamma(t)$ for trajectory 2 increases monotonically during the collision. The final rotational angular momentum j is given by[7]

$$j = -\frac{1}{\hbar}\int_{-\infty}^{\infty}\frac{\partial V}{\partial \gamma}dt \ . \tag{11}$$

The time dependence of the integrand $\partial V/\partial\gamma$ is apparently different for the two trajectories, which is shown in Fig. 13(d). As a result, the final angular momentum j for trajectory 1 is approximately 120 higher than that of trajectory 2 as shown in Fig. 13(e). For the homonuclear molecule N_2, the function $\partial V/\partial\gamma$ is represented by

$$\frac{\partial V}{\partial \gamma} = \frac{1}{2}Rr_{23}\sin|\gamma|\left[\frac{1}{r_{12}}\frac{\partial V}{\partial r_{12}} - \frac{1}{r_{31}}\frac{\partial V}{\partial r_{31}}\right] . \tag{12}$$

For these two trajectories, the interaction potential of the ion-molecule system is dominated by the ion-atom interaction of the closest pair during the collision, $V(R,\gamma)\simeq V(r_{12})$, so that $(1/r_{31})(\partial V/\partial r_{31})\simeq 0$. Furthermore, the function $(1/r_{12})(\partial V/\partial r_{12})$ as well as r_{12} is almost the same for the two trajectories. The difference in

the final rotational angular momentum j, therefore, comes from the difference in the function $|\gamma(t)|$. Although the CT calculations for the two selected trajectories are presented here in detail, this result is true for the trajectories at other γ_c's, even in the three-dimensional collisions. We therefore conclude that the split of rotational rainbow is due to the "orientational effect" in the angular momentum transfer.

The angular momentum transfer takes place in a narrow range of the intermolecular distance R around the turning point as can be seen in Figs. 13(a) and 13(e). For trajectories of $\gamma_c > 0°$, the variation of $\gamma(t)$ with time is small during the collisions, and the sudden condition is fulfilled. This would be the reason for the fact that the energy-loss position of rainbow peak (2) in the spectra can be estimated well with the simple hard-shell model.

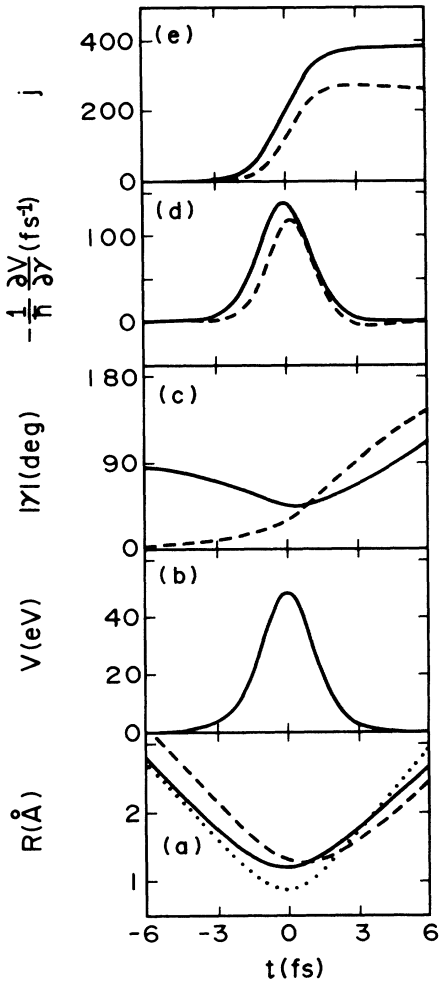

FIG. 13. Time dependence of two selected trajectories indicated by arrows in Fig. 12. (a) Intermolecular distance R; (b) interaction potential V; (c) molecular orientation angle $|\gamma|$; (d) derivative $-\hbar^{-1}(\partial V/\partial\gamma)$; and (e) rotational angular momentum j. The solid and dashed curves represent the scattering parameters for the trajectories at maxima (2) and (2′) in Fig. 12, respectively. The dotted curve in (a) indicates interatomic distance r_{12}. The time evolutions of V and r_{12} are both indistinguishably the same for these two trajectories.

For the trajectories of $\gamma_c < 0°$, on the other hand, the function $\gamma(t)$ depends strongly on the time t, and the angular momentum transfer cannot be evaluated in such a simple manner.

B. Vibrational excitation

Vibrational excitation takes place exclusively around the molecular orientation $\gamma_c = 0°$ and 90°, while rotational excitation does around $\gamma_c \simeq 50°$.[14,15] Vibrational excitation around $\gamma_c = 0°$ contributes only weakly to the energy-loss spectra because of the geometrical factor $\sin\gamma_c$ in Eq. (10). The effect of vibrational excitation on the energy-loss spectra, therefore, arises from the collisions around the molecular orientation of $\gamma_c = 90°$.

For collisions at $\gamma_c = 90°$, the two different trajectories, which are exhibited schematically in Fig. 14, belong to a certain scattering angle θ. These trajectories in Figs. 14(a) and 14(b) denote the collisions at the initial polar angles of $\alpha = 90°$ and 0°, respectively. In both cases the projectile is in the x-y plane during the collision. Figure 15 exhibits the time dependence of the scattering parameters for the trajectory of Fig. 14(a). The interaction potential $V(t)$ in the figure shows a flat maximum which is due to double collisions.[40–42] As can be seen in Figs. 15(d) and 15(e), in the first interaction the quantity $-\hbar^{-1}(\partial V/\partial\gamma)$ is positive and the angular momentum is transferred to the molecule. In the second collision, however, the quantity $-\hbar^{-1}(\partial V/\partial\gamma)$ is negative and the angular momentum, which was transferred to the molecule in the first impact, is turned back completely to the projectile. As a result of these interactions, the final angular momentum j transferred to the molecule is zero for this specific trajectory. In the case of the trajectory in Fig. 14(b), no torque acts on the molecule during the collision, and the final angular momentum $j = 0$. The final angular momentum j is exactly zero for these two trajectories, while all other trajectories, which belong to the collisions at a scattering angle θ, take finite j values.

The variation of the angular momentum with time $j(t)$ is completely different between the trajectories in Figs. 13 and 15. For the typical single-collision cases in Fig. 13, the angular momentum j_c at the turning point has ap-

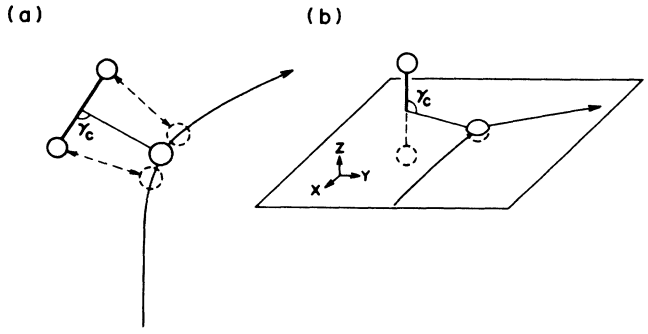

FIG. 14. Schematic drawing of two trajectories for the scattering at $\gamma_c = 90°$. (a) Typical double collision and (b) single collision.

proximately half the value of the final momentum j. In the double collisions, on the other hand, the function $j(t)$ takes a maximum value at the turning point (see Fig. 15). To distinguish the two vibrational excitation mechanisms around $\gamma_c = 90°$, the rotational angular momentum j_c at the turning point was compared with the final angular momentum j for each trajectory. If the angular-momentum difference $(j - j_c)$ was negative, the collision was considered to be double collisions. The trajectories which were regarded for the single collision were also classified according to the signs of j_z. Dashed curve C in Fig. 9(b), which is computed with the rigid-rotor model, exhibits the partial spectrum for double collisions. This result indicates that the peak located at the elastic position is predominantly due to double collisions, which coincides with the discussion on Xe-CO_2 collisions at low energy.[3] Curves A and B in Fig. 9(b) correspond to the single collisions of $j_z \geq 0$ and $j_z < 0$, respectively. The dashed curves in Fig. 9(c), which is the result of vibrotor calculation, denote the three components similar to those of Fig. 9(b). Contrary to Fig. 9(b) by the rigid-rotor calculation, curve C in Fig. 9(c) shows a broad structure with a flat maximum due to vibrational excitation, moreover, the additional peak d can be seen in curve A. Peaks d and b are located at nearly the same energy loss, so that a prominent peak appears in the middle of the spectrum. The similar analysis of the spectra in Fig. 10 and of the vibrotor calculations for $E_{lab} = 275$ and 350 eV indicates that the drastic change of the spectral structure around $\tau \simeq 8$ keV deg is concluded to be due to the appearance of additional peak d, which is similar to that in Fig. 9(c).

The appearance of additional peak d in Fig. 9(c) can be explained with the excitation function $\Delta E(\gamma_c)/E$ determined from the trajectories belonging to partial spectrum A. Figure 16 shows the excitation function $\Delta E(\gamma_c)/E$ for single collisions obtained with the vibrotor CT calculation for the collision energies of $E_{lab} = 150$, 200, and 250 eV at laboratory angle $\theta = 35°$. The maximum around $\gamma_c = 45°$ is due to the angular momentum transfer, and the maximum height is almost the same with that obtained by the rigid-rotor CT calculation. In the rigid-rotor model the energy $\Delta E/E$ at $\gamma_c = 0°$ and 90° is zero. The finite values of the excitation energy at $\gamma_c = 0°$ and 90° in the vibrotor model are due to vibrational excitation.

In the spectra computed for $E_{lab} = 150$ and 200 eV and at $\theta = 35°$, the additional peak d in partial spectrum A does not appear distinctly. The excitation function for $E_{lab} = 250$ eV in Fig. 16 shows a minimum around $\gamma_c = 80°$, while the other two functions do not show it. Peak d in curve A in Fig. 9(c) is, therefore, ascribed to

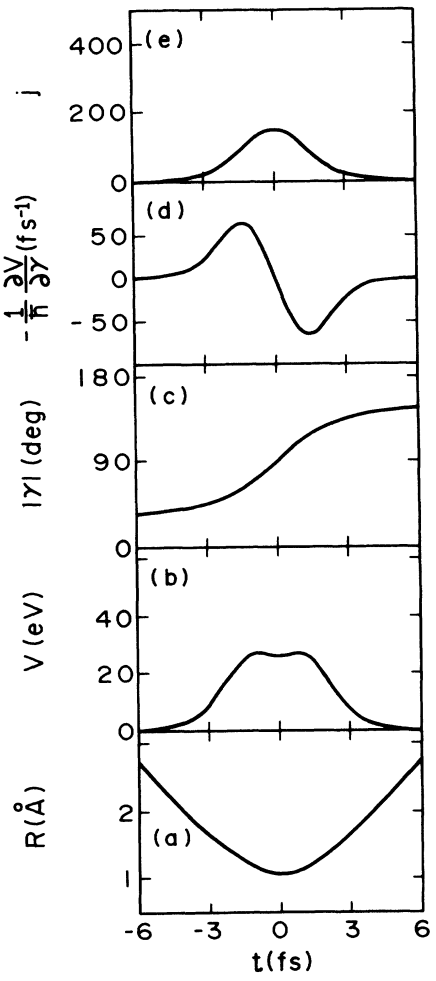

FIG. 15. Time dependence of a typical trajectory for the double collision, $\gamma_c = 90°$, at $E_{lab} = 175$ eV and $\theta = 35°$.

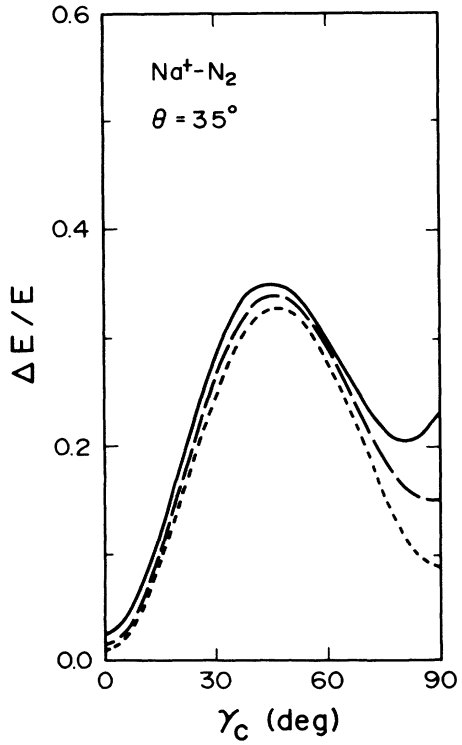

FIG. 16. Excitation function $\Delta E(\gamma_c)/E$ for the single collisions of $j_z \geq 0$ calculated with the vibrotor model at $\theta = 35°$. The solid, dashed, and dotted curves are for $E_{lab} = 250$, 200, and 150 eV, respectively.

the minimum in the excitation function around $\gamma_c = 80°$, and is considered to be a rainbow peak. All the structures in the spectra simulated for $E_{lab} = 275$ and 350 eV are also explained quite well by decomposing each spectrum into three components A, B, and C as in Fig. 9(c). According to these analyses of the spectra, the structural change of the energy-loss spectra at $\tau_c \simeq 8$ keV deg is due to the fact that the single-collision excitation function $\Delta E(\gamma_c)/E$ takes a minimum around $\gamma_c = 80°$, which forms a new rainbow peak in the spectra.

V. SUMMARY

The angular and energy dependences of the energy loss spectra measured for the impulsive Na^+-N_2 collisions were analyzed with the classical trajectory calculations on the simple additive interaction potential surface. The CT calculations reproduce satisfactorily the experimental finding in this study. The energy-loss spectra observed at lower energy $E_{lab} < 200$ eV can be simulated fairly well with the CT calculation of the rigid-rotor model. The triple-peak structure in the spectra observed at these lower energies are explained in terms of rotational rainbow, by taking into account the direction of the final angular momentum vector j.

The spectra measured at higher energies and larger angles were reproduced satisfactorily only with the CT calculation of the vibrotor model. This suggests that the contribution of vibrational excitation in the momentum transfer is significant under these experimental conditions. Nevertheless, the largest energy transfer in the spectra is still determined predominantly by the angular momentum transfer. This is due to the fact that the angular momentum transferred to the molecule in the collisions around the rainbow angle $\gamma_c \simeq 45°$ is quite big in the Na^+-N_2 system studied here.

ACKNOWLEDGMENTS

One of the authors (S.K.) wishes to thank Dr. R. Schinke (Max-Planck-Institut für Strömungsforschung, Göttingen, West Germany) for pointing out the possibility of a split of the rotational rainbow in a collision system with large anisotropy. We are grateful for valuable discussions with Professor H. Inouye (Bunri University Tokushima, Tokushima, Japan). Professor Y. Sato (Tohoku University, Sendai, Japan) and Dr. M. Nakamura (Institute for Molecular Science, Okazaki, Japan). This work was supported financially in part by a Grant-in-Aid for Scientific Research from the Ministry of Education, Science and Culture of Japan.

[1] M. Faubel, Adv. At. Mol. Phys. **19**, 345 (1983), and references therein.
[2] W. Schepper, U. Ross, and D. Beck, Z. Phys. A **290**, 131 (1979).
[3] U. Buck, D. Otten, R. Schinke, and D. Poppe, J. Chem. Phys. **82**, 202 (1985).
[4] E. Gottwald, A. Mattheus, and K. Bergmann, J. Chem. Phys. **86**, 2680 (1987).
[5] D. Beck, U. Ross, and W. Schepper, Z. Phys. A **293**, 107 (1979).
[6] S. Bosanac, Phys. Rev. A **22**, 2617 (1980).
[7] H. J. Korsch and R. Schinke, J. Chem. Phys. **73**, 1222 (1980).
[8] M. Faubel, J. Chem. Phys. **81**, 5559 (1984).
[9] K. Raghavan, N. Sathyamurthy, and B. A. Garetz, Chem. Phys. **113**, 187 (1987).
[10] U. Hefter, P. L. Jones, A. Mattheus, J. Witt, and K. Bergmann, Phys. Rev. Lett. **46**, 915 (1981).
[11] R. Schinke and J. M. Bowman, in *Molecular Collision Dynamics*, edited by J. M. Bowman (Springer-Verlag, Berlin, 1983).
[12] H. J. Korsch and R. Schinke, J. Chem. Phys. **75**, 3850 (1981).
[13] M. Nakamura, J. Phys. Soc. Jpn. **56**, 3145 (1987).
[14] T. Hasegawa, S. Kita, M. Izawa, and H. Inouye, J. Phys. B **18**, 3775 (1985).
[15] M. Nakamura, S. Kita, and T. Hasegawa, J. Phys. Soc. Jpn. **56**, 3161 (1987).
[16] U. Gierz, J. P. Toennies, and M. Wilde, Chem. Phys. Lett. **110**, 115 (1984).
[17] G. Ziegler, M. Rädle, O. Pütz, K. Jung, H. Ehrhardt, and K. Bergmann, Phys. Rev. Lett. **58**, 2642 (1987).
[18] Z. Bacic and S. D. Bosanac, Phys. Rev. A **30**, 2998 (1984).
[19] S. Kita, T. Hasegawa, A. Kohlhase, and H. Inouye, J. Phys. B **20**, 305 (1987).
[20] R. Schinke, J. Chem. Phys. **85**, 5049 (1986).
[21] K. Sato, Y. Achiba, H. Nakamura, and K. Kimura, J. Chem. Phys. **85**, 1418 (1986).
[22] Y. Sato, K. Niurao, H. Takagi, and H. Inouye, J. Chem. Phys. **65**, 3952 (1976).
[23] N. Andersen, M. Vedder, A. Russek, and E. Pollack, Phys. Rev. A **21**, 782 (1980).
[24] S. J. Martin, V. Heckman, E. Pollack, and R. Snyder, Phys. Rev. A **36**, 3113 (1987).
[25] P. Sigmund, J. Phys. B **14**, L321 (1981).
[26] S. Kita, H. Tanuma, and M. Izawa, Chem. Phys. (to be published).
[27] H. Van Dop, A. J. H. Boerboom, and J. Los, Physica (Utrecht) **54**, 223 (1971).
[28] P. F. Dittner and S. Datz, J. Chem. Phys. **54**, 4228 (1971).
[29] K. T. Gillen, B. H. Mahan, and J. S. Winn, Chem. Phys. Lett. **22**, 344 (1973).
[30] J. Schöttler and J. P. Toennies, Chem. Phys. **2**, 137 (1973).
[31] W. L. Dimpfl and B. H. Mahan, J. Chem. Phys. **60**, 3238 (1974).
[32] M. Faubel and J. P. Toennies, Chem. Phys. **4**, 36 (1974).
[33] H. Inouye, M. Izawa, S. Kita, K. Takahashi, and Y. Yamato, Bull. Res. Inst. Sci. Meas. Tohoku Univ. **32**, 41 (1984).
[34] M. Izawa, S. Kita, and H. Inouye, J. Appl. Phys. **53**, 4688 (1982).
[35] S. Kita and H. Inouye, J. Phys. B **12**, 2339 (1979).
[36] K. P. Huber and G. Herzberg, *Molecular Spectra and Molecular Structure IV. Constants of Diatomic Molecules* (Van Nos-

trand Reinhold, New York, 1979).
[37]T. Ishikawa, S. Kita, and H. Inouye, Bull. Res. Inst. Sci. Meas. Tohoku Univ. **24**, 101 (1976).
[38]R. A. LaBudde and R. B. Bernstein, J. Chem. Phys. **55**, 5499 (1971).
[39]M. Karplus, R. N. Porter, and R. D. Sharma, J. Chem. Phys. **43**, 3259 (1965).
[40]A. L. Boers, Surf. Sci. **63**, 475 (1977).
[41]I. Kusunoki and Ch. Ottinger, J. Chem. Phys. **70**, 710 (1979).
[42]S. Bosanac, Phys. Rev. A **26**, 816 (1982).